Image Metrics for Deconvolution of Satellites in Low Earth Orbit

Sierra Hickman[1,*], Vishnu Anand Muruganandan[1], Stephen Weddell[1], and Richard Clare[1]

[1]Department of Electrical and Computer Engineering, University of Canterbury, Christchurch, New Zealand
[*]*Corresponding Author: sierra.hickman@pg.canterbury.ac.nz*

***Abstract*—Satellites and space debris clutter low Earth orbital paths. This causes concerns for future launches as the clutter increases the probability of in-orbit collisions. Therefore, it is important to track and characterise these objects. However, the Earth's atmosphere distorts images collected from ground-based telescopes. The blurring effects of the atmosphere can be reduced through post-processing deconvolution to improve the images of satellites and space debris. Yet, a metric is needed to quantify the quality of the images and deconvolution of these extended objects at finite distances; as well as to characterise the structure and brightness for un-symmetrical satellites in low Earth orbit. This paper uses images collected of the International Space Station to investigate the use of the structural similarity metric and the regional properties as potential satellite imaging metrics. Our results show that the similarity metric is useful to characterise the orientation of the satellite relative to the observer, while the regional properties serve to quantify the image quality and improvement due to deconvolution.**

I. Introduction

Since the start of the space age in 1957, about $9,600$ satellites have been launched. As of February 2020, $5,500$ satellites are still in orbit; of which only $2,300$ are still functioning [1]. Due to these dead satellites and increased space activity in recent years, the amount of space debris in low Earth orbit (LEO) has increased exponentially. Currently, $42,000$ objects are in orbit; of which only $23,000$ are regularly tracked and catalogued by the US Space Surveillance Network [2]. Since collisions can be devastating to both functioning satellites and rocket launches, it is crucial to track and characterise these objects to detect and avoid any future collisions.

Unfortunately, the layers of Earth's atmosphere are composed of several pockets of different temperatures and humidity levels which constantly move and mix together, causing fluctuations in the index-of-refraction of the air [3]. As a result, the light travelling through the atmosphere experiences a non-uniform optical path. Therefore, any object observed through the atmosphere will experience a wavefront distortion and, in turn, reduction in image quality. Image resolution loss hinders not only astronomers [4], but also anyone within space situational awareness and space traffic management.

A computer post-processing technique called deconvolution digitally corrects for the effects of the turbulent atmosphere after an image is collected from a ground-based telescope [5]. However, current astronomical imaging techniques utilise imaging metrics that are dependent on stars, which are symmetrical point-sources at infinite distances. A system is needed to process and characterise images of extended, un-symmetrical, LEO satellites. This paper investigates the use of two imaging metrics, the structural similarity metric and the regional properties, to characterise satellite observations. Specifically, the International Space Station (ISS) is imaged using the Boller and Chivens (B&C) optical telescope at Mount John University Observatory (MJUO) using a background star to estimate the atmospheric turbulence.

Section II introduces the theoretical background of the atmospheric imaging problem, Lucy-Richardson and blind deconvolution, and summarises the important imaging metrics. The method used to collect ISS images is explained in Section III. The process and experiment of the similarity metric are described in Section IV. Section V details the deconvolution process. Then the regional properties experiment is outlined in Section VI. A comparison of the results for the two imaging metrics are examined in Section VII. Finally, Section VIII concludes with final remarks and an outline for future works.

II. Background

A. Imaging and Deconvolution

The images collected through the atmospheric turbulence are described mathematically as

$$d = o \odot h + n, \tag{1}$$

where d is the observed image, o is the original object unperturbed by the turbulence, h is the perturbing Point Spread Function (PSF) of the atmosphere, and n is noise on the data [5]. The operator $\odot$ indicates convolution. Deconvolution utilises the blurred image, an assumption or constraints of the PSF, and properties of the noise to recover the original object. In the specific case of a single point-source, like a far-away star, and the complete absence of noise, the PSF of the atmosphere would resemble the spread and shape of the star in a blurred image.

Deconvolution algorithms restore the original object image by minimising the effects of the turbulence. One such algorithms is the Lucy-Richardson iteration [6]. It uses an iterative process to restore an image blurred by a known PSF by converging to a maximum likelihood solution. Mathematically, it is defined as [7],

$$\hat{o}^{(k+1)} = \hat{o}^{(k)} \left(\hat{h}^* \otimes \frac{d}{\hat{o}^{(k)} \otimes \hat{h}} \right), \tag{2}$$

where $\hat{o}^{(k)}$ is the kth iteration estimate of the original image, $\hat{h}$ is an estimate of the PSF, and $\hat{h}^*$ is the flipped PSF. The symbol $\otimes$ is the correlation operator. For the first iteration, $\hat{o}^{(0)} = d$. Typically, the PSF is estimated by utilising a wavefront sensor to measure the fluctuations of a background star [8]. Instead, this study uses the spread of a single background star as the PSF estimate.

Blind deconvolution [9] is utilised when both the original image, o, and the blurring PSF, h, are unknown. There is no wavefront sensor to estimate the wavefront distortion, and images are restored solely with the information present in the blurred image, d. An initial "blind" estimation of the PSF serves as a starting-point for the deconvolution process. This blind estimation is usually created from *a priori* knowledge or assumptions about the original image or atmosphere. A modification of the Lucy-Richardson algorithm [10], or other iterative algorithms [11]–[13], are then utilised to continually refine the blind PSF estimation. The algorithms converge to a maximum likelihood PSF and recovered image. This study uses the iterative blind deconvolution method described by Biggs [13], which is conveniently found in Matlab's *deconvblind* function [14]. We also use the spread of a single background star as the "blind" PSF estimate.

B. Imaging Metrics

The Full-Width at Half-Maximum (FWHM) metric is commonly used to quantify image quality or characterise the atmospheric turbulence [15]. By definition, the FWHM is the width of a signal at half of its maximum value. This metric is usually applied to images of stars, where a Gaussian curve is fit to the star's intensity profile and the FWHM of the Gaussian fit is measured. Imaging systems, like those using adaptive optics and deconvolution, aim to reduce the FWHM of stars.

While the FWHM is valid for point-sources like stars, it is not as meaningful with extended objects like satellites. For example, a FWHM metric will indicate an improvement to a satellite image even if deconvolution incorrectly eliminates part of the satellite signal. Therefore, another imaging metric is needed for extended space objects. We propose two possible contenders: the similarity metric and regional properties.

The similarity metric was created by Wang et al. [16] and compares two images. It utilises three independent comparison functions: luminance $l(\boldsymbol{x_1}, \boldsymbol{x_2})$, structure $s(\boldsymbol{x_1}, \boldsymbol{x_2})$, and contrast $c(\boldsymbol{x_1}, \boldsymbol{x_2})$. Combining the three comparison functions produces the structural similarity metric,

$$S(\boldsymbol{x_1}, \boldsymbol{x_2}) = [l(\boldsymbol{x_1}, \boldsymbol{x_2})]^{\alpha} \cdot [c(\boldsymbol{x_1}, \boldsymbol{x_2})]^{\beta} \cdot [s(\boldsymbol{x_1}, \boldsymbol{x_2})]^{\gamma}, \quad (3)$$

where $\boldsymbol{x_1}$ and $\boldsymbol{x_2}$ are two images; and $\alpha > 0$, $\beta > 0$, and $\gamma > 0$ alter the relative weighting of the three comparison functions. Wang et al. define the three comparison functions,

$$\begin{aligned} l(\boldsymbol{x_1}, \boldsymbol{x_2}) &= \frac{2\mu_{x1}\mu_{x2} + C_1}{\mu_{x1}^2 + \mu_{x2}^2 + C_1} \\ c(\boldsymbol{x_1}, \boldsymbol{x_2}) &= \frac{2\sigma_{x1}\sigma_{x2} + C_2}{\sigma_{x1}^2 + \sigma_{x2}^2 + C_2} \\ s(\boldsymbol{x_1}, \boldsymbol{x_2}) &= \frac{\sigma_{x1x2} + C_3}{\sigma_{x1}\sigma_{x2} + C_3}, \end{aligned} \quad (4)$$

where μ_{x1}, μ_{x2}, σ_{x1}, σ_{x2}, and σ_{x1x2} are the local means, standard deviations, and cross-covariance for the two images. C_1, C_2, and C_3 are all constants. Using $\alpha = \beta = \gamma = 1$ and $C_3 = C_2/2$, Equation 3 simplifies to

$$S(\boldsymbol{x_1}, \boldsymbol{x_2}) = \frac{(2\mu_{x1}\mu_{x2} + C_1)(2\sigma_{x1x2} + C_2)}{(\mu_{x1}^2 + \mu_{x2}^2 + C_1)(\sigma_{x1}^2 + \sigma_{x2}^2 + C_2)}. \quad (5)$$

The resulting similarity value ranges from 0 to 1, where 1 is a perfect match between the two images. If one image is considered to be of perfect quality (i.e. not perturbed by atmospheric turbulence), then the similarity metric can quantify the quality of the second image [16].

Possible regional properties extracted from the satellite images are length, width, area, and brightness. The image dimensions of the ISS are based on the number of pixels across the signal. However, the physical dimensions of the ISS are in metres; therefore the spatial resolution of the image is used to convert the pixel dimensions to metres. The spatial resolution, SR, is defined as,

$$SR = \frac{p \times r}{f}, \quad (6)$$

where p is the physical width of the pixel, r is the range or distance between the telescope and the satellite, and f is the focal length of the telescope. The physical length, l, and width, w, of the satellite in the image is determined using

$$l = a_{major} \times SR \quad (7)$$

$$w = a_{minor} \times SR \quad (8)$$

where a_{major} is the number of pixels along the major axis, and a_{minor} is the number of pixels along the minor axis. Since the size of the ISS is known, the estimated ISS length and width from the image can be compared to the actual dimensions. The accuracy of the estimations to the real dimensions will indicate the validity of the regional properties as a satellite imaging metric. It is important to validate the regional properties method on a known satellite before moving to LEO debris, where the actual dimensions may be unknown. If validated, the regional properties can be used to characterise the size of various LEO debris.

III. Satellite Observation

The B&C telescope has a diameter of 0.61m and a focal ratio of either 6.25 or 13.5 [17]. We use the focal ratio of 6.25 which has a focal length, f, of 3.85m. Our detector, the FLIR Grasshopper (GS3), has a sensor width of 11.3mm and pixel width, p, of 5.5 μm [18]. The ISS was observed on 26th May 2020 at 07:32:27 (NZST).

The ISS orbits Earth at an altitude of 418km [19], and has an angular velocity of 63 arcminutes/s (7.6 km/s). During the observation, the ISS was at an elevation of 31°, which corresponds to a range, r, of 778 km. The resulting observational Field-of-View (FoV) is 20 arcminutes. Therefore, the ISS passes over the FoV in 0.3s.

Due to the high angular velocity of the ISS, the image would suffer motion blur at a long exposure. However, a low exposure

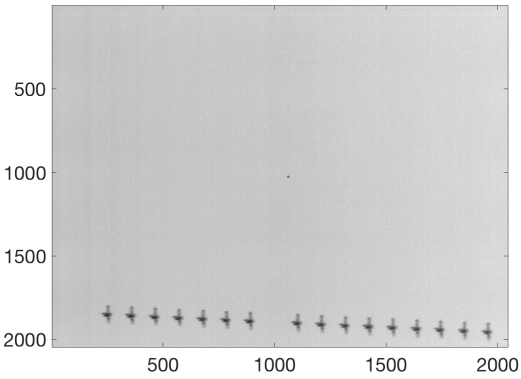

Fig. 1: Frames 203 – 218, of the captured image series where the ISS is in the FoV, stacked together. The background star, HIP 58905, is located in the centre of the image. Due to a limited streaming bandwidth, two frames were not captured.

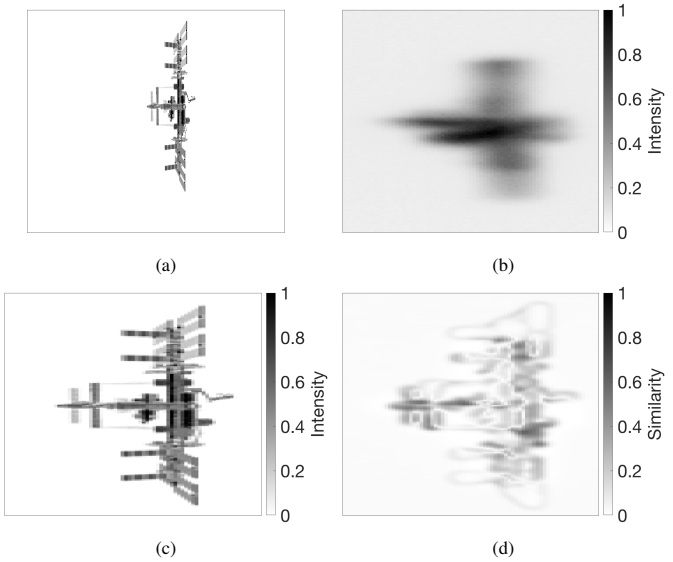

Fig. 2: The a) high resolution ISS model image, b) on-sky ISS image (Frame 210), c) trimmed and pixelated model image, and d) resulting similarity map. The signal intensities for images b, c, and d are normalised to a range of $0 - 1$.

would result in too low of a signal-to-noise ratio. Therefore, the exposure time was set to 2ms at a framerate of 60 frames/s. The angle between the sun, satellite, and telescope has to be around $90°$ to obtain the maximum reflected sunlight. This condition occurs during sunset and sunrise, therefore the ISS was observed just before sunrise at an angle of $97°$.

Typically, the ISS is visible for about ten minutes when passing over MJUO. A satellite tracking system is required to observe the ISS continuously over the entire pass. However, MJUO does not have a satellite tracking system. As a result, the telescope is pointed to a particular location of the satellite trajectory. The ISS is imaged as it passes over the set telescope position's FoV. A position along the satellite trajectory is selected with a bright near-by background star. The background star, HIP 58905, which has an apparent magnitude of 5.0, is used as a PSF estimate during deconvolution in Section V. Fig. 1 consists of the sum of all the frames containing the ISS; the background star is seen at the centre of the image.

IV. Similarity Metric

A. ISS Model Orientation

As described in Section II-B, the similarity metric needs a reference image of perfect quality. Since we do not have a way to directly observe the ISS without the atmosphere from our location, we must simulate an unperturbed image of the ISS. The unperturbed image created is based on the orientation of the satellite in the collected on-sky images.

First, the frames from the 26 May 2020 on-sky observation in which the ISS was present on the detector were identified. A single frame from the identified images was selected from the centre of the series. In the selected frame (Frame 210), the ISS is closest to the centre of the image. A close-up of the ISS signal on Frame 210 is seen in Fig. 2b.

LightWave [20] is used to manipulate a 3D model of the ISS. The model is located in the NASA on-line archives as a ".lws" file [21]. The ISS model is rotated along three axes to find several plausible viewing angles which appear similar to the selected observation frame. The Solar Alpha Rotary Joints [22] are also rotated on the ISS model to match the solar arrays of the observed ISS. LightWave allows for high precision control of the three main rotations and rotary joints, which permit repeatability and fine incremental changes.

B. Similarity Process

Once a suitable viewing angle is established, a high resolution image of the ISS model is rendered. The high resolution model image is then processed with an identified on-sky ISS frame. We input the ISS signal's starting and ending pixel positions along the row and column directions for both the high resolution model and original on-sky images. The pixel ratio of the on-sky ISS signal to the high resolution model ISS signal for the length and width dimensions are then averaged. The average ratio is used to pixelate the high-resolution model image using Matlab's *imresize* function [14]. As a result, the pixel dimensions of the ISS signal regions are similar for both the pixelated model and on-sky images. Extra pixels around the identified ISS signal regions are then included to buffer the signals and reduce accidental information loss. The buffered regions are then extracted to create the on-sky ISS image and trimmed model image.

Using Frame 210 for example, the ISS signal is about 105 pixels long and 60 pixels wide in the on-sky image, and 368 pixels long and 107 pixels wide in the original high resolution model (Fig. 2a). The on-sky to high resolution model ratio is about 0.56 for the width and 0.28 for the length. The average ratio is then about 0.42. The high resolution model image is reduced in resolution by $\frac{1}{0.42}$ to produce a pixelated image. In the pixelated image, the ISS signal is about 45 pixels wide and 155 pixels tall. A region of 171x78 pixels is extracted from both the pixelated model and original on-sky images centering around the ISS signals, producing the

on-sky ISS image (Fig. 2b) and trimmed and pixelated model image (Fig. 2c).

The resulting images are both normalised to a maximum pixel intensity of 1. They are then passed through Equation 5 using Matlab's *ssim* function [14] to calculate the structural similarity of the on-sky ISS image to the trimmed model image. A similarity map for each pixel region, and a mean similarity value are produced. The resulting similarity map from Frame 210 is seen in Fig. 2d.

The similarity metric is sensitive to pixel misalignment. Therefore, the similarity process was performed over several iterations, translating the on-sky ISS image up to +/- 15 pixels (incrementing by 1 pixel) along the row and column directions. The row and column positions which resulted in the maximum similarity value are assumed to be the correct pixel alignments and are used for recorded results. Finally, the entire similarity metric process is repeated for every frame with the ISS from the 26 May 2020 on-sky observation series.

C. Nearest Orientation Match

The actual ISS orientation relative to the observer and telescope is unknown. This uncertainty allows for many ISS model orientations to be possible matches to the observed ISS images. Therefore, the process described in Section IV-B is performed for several different ISS model viewing angles.

Four main viewing angles which are visually similar to the observed ISS orientation are used. The viewing angle closest to the actual ISS orientation will result in the highest similarity value. The four model viewing angles are seen in Fig. 3, and are compared to the on-sky ISS image seen in Fig. 2b. The best-fit ISS model viewing angle is Fig. 3b, which has a similarity value of 0.0558. This viewing angle was used in Fig. 2, and will be used for the remainder of this study regarding the similarity metric.

V. Deconvolution

Satellite deconvolution is performed to improve the on-sky ISS images. The background star and ISS are extracted from the original on-sky image. The extracted regions are larger than the on-sky ISS image used for the similarity metric. Both regions have the same dimensions of 201x201 pixels. The background star region creates the PSF estimate. Since the star is a point-source which has been perturbed by the Earth's atmosphere, the spread of the background star can serve as the PSF estimate for the deconvolution (as discussed in Section II-A). However, since the atmosphere is continually evolving during the observation, a new PSF estimate is extracted for each frame of the series. Each PSF is normalised to have a total integrated intensity of 1, and passed as the initial PSF estimate for the Lucy-Richardson and blind deconvolution. Before deconvolution, both the PSF and the on-sky ISS image are converted from 8-bit to float values. Both deconvolution methods were performed for every frame of the observation with the ISS in view. After deconvolution, both the similarity metric (Section IV-B) and regional properties method (Section VI) are executed for every deconvolved image.

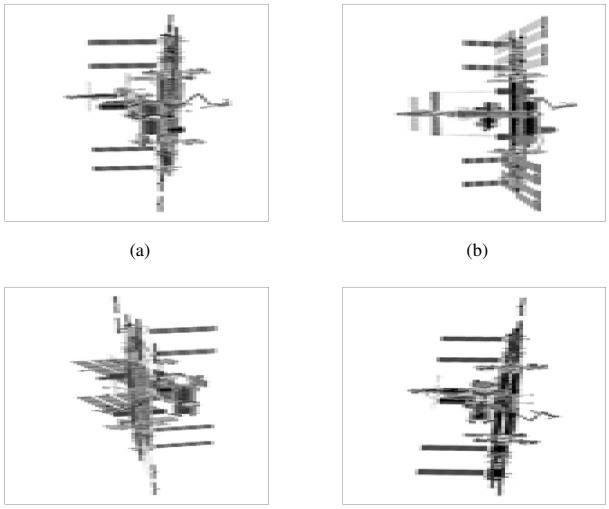

Fig. 3: Different ISS model viewing angles processed through the similarity metric. The resulting similarity values to the on-sky ISS image (Frame 210) are a) 0.0486, b) 0.0558, c) 0.0533, d) 0.0420.

The Lucy-Richardson deconvolution was performed with 30 iterations. It was found that increasing the number of iterations past 30 did not yield a significant increase in the deconvolved similarity value, and would eventually lead to information loss as the solar arrays on the ISS would be eliminated from the final deconvolved image at higher iterations. The initial PSF estimate for the blind deconvolution was the background star region, however the function eventually landed on a PSF with less background noise after 10 iterations. An example of the on-sky ISS image, the corresponding PSF, and the resulting deconvolved images for each method on a Frame 210 can be seen in Fig. 4.

We had two main theories regarding the deconvolution of the ISS images. First, a successful satellite deconvolution would result in an improved image metric, either the similarity metric value or any of the regional properties. Ideally, an improvement to both image metrics would be observed as this would provide for double confirmation and validation of the deconvolution method. Second, the similarity value and regional properties would experience larger improvements in frames where the ISS is closest to the background star. In theory, the background star and ISS signal are encountering more of the same volume of atmospheric turbulence when they are closer together, a concept known as angular anisoplanatism [23]. As a result, the PSF of the star would more closely resemble the actual turbulence experienced by the ISS signal.

VI. Regional Properties

For the regional property imaging metric, the spatial resolution of the on-sky image has to be determined. The spatial resolution of the ISS imaged is estimated using Equation 6. Theoretically, the spatial resolution or diffraction limit of the ISS during the observation is 1.11 metres. However, the theoretical spatial resolution of the image cannot be achieved

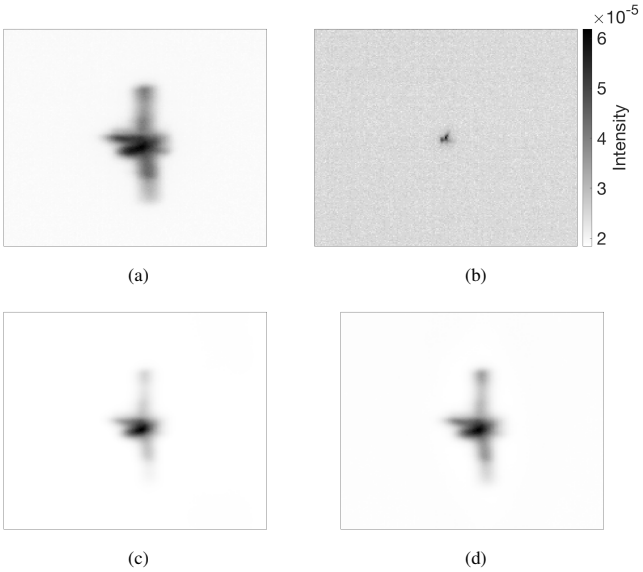

Fig. 4: The a) pre-deconvolved on-sky ISS image, b) the extracted PSF of the background star, and the final deconvolved images after c) Lucy-Richardson and d) blind deconvolution of Frame 210. The total intensity of the PSF is normalised to equal 1.

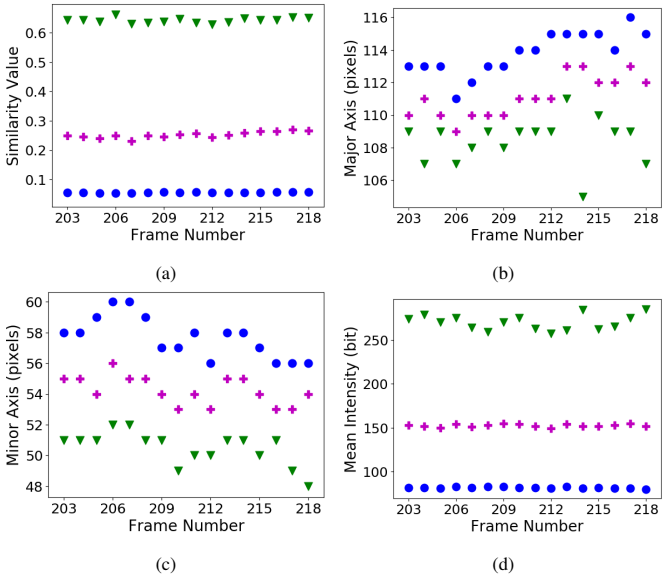

Fig. 5: a) Similarity value of the ISS to the best-fit model orientation. b) Length of the Major axis of the ISS image. c) Length of the Minor axis of the ISS image. d) Average intensity of the ISS image. Blue circle data points are from before deconvolution, and green triangle and magenta plus data points are from after Lucy-Richardson and blind deconvolution respectively.

due to the atmospheric distortion and motion blur. Therefore, as discussed in Section V, the deconvolution performed aimed to reduce the atmospheric effects.

The regional properties of the ISS are first estimated for the pre-deconvolved on-sky images. The mean intensity and standard deviation, σ, of the image is measured. A threshold of 6σ is used to remove the background noise from the image. Afterwards, pixels with connected components are grouped using Matlab's *bwconncomp* function [14]. Groups containing between 9 and $5,000$ pixels are labelled as objects. The number of pixels is measured along the major and minor axis of the labelled object, and its average pixel intensity is calculated using Matlab's *regionprop* function [14]. These properties yield structural information of the ISS, which are then compared to the real dimensions of the satellite to estimate the accuracy of the regional properties metric.

The aforementioned regional properties process is repeated for every frame with the ISS from the 26 May 2020 on-sky observation series, before and after deconvolution. The average number of pixels in both the major and minor axis is calculated, then substituted into Equations 7 and 8 respectively to estimate the dimensions of the ISS. The estimated dimensions are then compared to the actual ISS length and width, which are 109m and 51m respectively [24].

VII. Results and Discussion

The similarity metric improved after deconvolution for both Lucy-Richardson and blind deconvolution, verifying that satellite deconvolution using the spread of the background star as the PSF does improve the images. On average, Lucy-Richardson and blind deconvolution experienced a $1,050\%$ and 350% increase in similarity value, respectively. The similarity value before and after each deconvolution for each frame with the ISS in view are shown in Fig. 5a.

TABLE I: The average regional properties of the ISS images. Ground truth are the physical dimensions of the ISS, Original are the measurements from the pre-deconvolved images, and L-R and Blind are short for Lucy-Richardson and blind deconvolution respectively.

	Ground Truth	Original	L-R	Blind
ISS Length (m)	109	126.5	119.8	123.2
ISS Width (m)	51	64.4	56.6	59.9
Average Intensity	–	82	270	153

The number of pixels measured in the major axis and minor axis, and the mean intensity of the ISS for each of the pre-deconvolved, Lucy-Richardson, and blind deconvolved frames are seen in Fig. 5b, 5c, and 5d respectively. The average number of pixels for both the major axis and minor axis are converted to physical lengths using Equations 7 and 8. The results are seen in Table I. In the pre-deconvolved images, the length and width of the ISS are 16% and 26% larger than the physical dimensions respectively. This is likely due to the motion blur of the ISS and the atmospheric turbulence. Lucy-Richardson and blind deconvolution experienced an average spatial resolution improvement of 11% and 6% respectively. The average intensity of the ISS is also enhanced by 229% and 87% for the Lucy-Richardson and blind deconvolution respectively. Therefore, the regional properties were able to confirm and quantify the image improvement after deconvolution.

It was theorised that the improvement of the similarity value and regional properties after deconvolution would be greatest when the satellite was at its closest to the background star, in Frame 210. However, such a trend cannot be clearly identified in Fig. 5. A possible explanation could be due to the varying

turbulence of the atmosphere. Certain frames in the series may have experienced worse turbulence than others, which would explain the non-uniform similarity values and regional properties before deconvolution across the different frames. It is also of note that the ISS crosses the detector laterally without passing close to the background star, as seen from Fig. 1, meaning the distance from the satellite to the background star does not change drastically with each frame. This trend may be noticeable for an observation where the ISS or satellite passes closer to the background star, or where the distance between the satellite and star changes more drastically between frames. The results for the similarity metric could also be improved by iterating over more angles for the ISS model to find a better fit. It is clear from Fig. 2 that the best-fit model used in this study could be improved.

VIII. Conclusion and Future Work

This study proposed use of regional properties and the similarity metric to quantify the image quality and deconvolution of satellite images. It has shown the similarity metric is a promising tool to measure and confirm satellite deconvolution improvement, although perhaps not as well as the regional properties method. However, the similarity metric is useful for identifying the orientation of the ISS or satellite in relation to the observer by utilising 3D models. It was also confirmed that the spread of the background star may be used as the PSF in astronomical deconvolution to improve observations of satellites.

Future work to extend this study would involve using a wavefront sensor–such as the geometric [25], curvature [26], or Shack-Hartmann [8]–to estimate the wavefront of the background star. As mentioned in Section II-A, the spread of the star would resemble the true PSF of the atmosphere only in the case of no noise. However, noise was present in the images collected, so our assumptions of the PSF were flawed. A wavefront sensor would improve the estimate of the PSF caused by the atmosphere. A more accurate PSF will in-turn result in a better deconvolved image. Also, the similarity metric could be improved by iterating the 3D model of the satellite over several more angles to identify a better fit. Another plan is to use a higher quality camera with a better quantum efficiency for future observations. This new camera allows for a shorter exposure time to observe the ISS or other satellites which will reduce motion blur. We also plan to extend this work to other satellites, such as the ENVISAT [27]. *A priori* knowledge of the imaged satellite's trajectory will be used to estimate the motion blur and further improve the on-sky images. Finally, this work will be incorporated into a proposed photometry-based image restoration system for near Earth objects at MJUO [28].

IX. Acknowledgements

The authors would like to acknowledge and thank the staff at Mt. John University Observatory. The observational trip to Mt. John was supported by the Marsden Fund Council from Government funding, administered by the Royal Society of New Zealand. Gratitude is also extended to Associate Professor Andrew Lambert for his counsel regarding the deconvolution, as well as Dr. Ian Griffin for his advice on imaging the ISS.

References

[1] European Space Agency. (2020) Space debris by the numbers. [Online]. Available: https://www.esa.int/Safety_Security/Space_Debris/Space_debris_by_the_numbers

[2] European Space Agency. (2020) About space debris. [Online]. Available: https://www.esa.int/Safety_Security/Space_Debris/About_space_debris

[3] F. Roddier, "The effects of atmospheric turbulence in optical astronomy," in *Progress in optics*. Elsevier, 1981, vol. 19, pp. 281–376.

[4] P. Hickson, "Atmospheric and adaptive optics," *The Astronomy and Astrophysics Review*, vol. 22, no. 1, p. 76, 2014.

[5] R. G. Lane, M. Tallon, E. Thiebaut, and R. M. Clare, "Diffraction limited image restoration by post-compensation from simultaneous speckle and wavefront sensing observations," in *Adaptive optical system technologies II*, vol. 4839. International Society for Optics and Photonics, 2003, pp. 1142–1153.

[6] W. H. Richardson, "Bayesian-based iterative method of image restoration," *JoSA*, vol. 62, no. 1, pp. 55–59, 1972.

[7] J.-L. Starck, E. Pantin, and F. Murtagh, "Deconvolution in astronomy: A review," *Publications of the Astronomical Society of the Pacific*, vol. 114, no. 800, p. 1051, 2002.

[8] J. M. Geary *et al.*, *Introduction to wavefront sensors*. Spie Press, 1995, vol. 18.

[9] T. G. Stockham, T. M. Cannon, and R. B. Ingebretsen, "Blind deconvolution through digital signal processing," *Proceedings of the IEEE*, vol. 63, no. 4, pp. 678–692, 1975.

[10] D. Fish, A. Brinicombe, E. Pike, and J. Walker, "Blind deconvolution by means of the richardson–lucy algorithm," *JOSA A*, vol. 12, no. 1, pp. 58–65, 1995.

[11] G. Ayers and J. C. Dainty, "Iterative blind deconvolution method and its applications," *Optics letters*, vol. 13, no. 7, pp. 547–549, 1988.

[12] B. Davey, R. Lane, and R. Bates, "Blind deconvolution of noisy complex-valued image," *Optics Communications*, vol. 69, no. 5-6, pp. 353–356, 1989.

[13] D. S. Biggs and M. Andrews, "Acceleration of iterative image restoration algorithms," *Applied optics*, vol. 36, no. 8, pp. 1766–1775, 1997.

[14] *MATLAB version 9.8.0.1380330 (R2020a) Update 2*, The Mathworks, Inc., Natick, Massachusetts, 2020.

[15] M. C. Roggemann and B. M. Welsh, *Imaging through turbulence*. CRC press, 1996.

[16] Z. Wang, A. C. Bovik, H. R. Sheikh, and E. P. Simoncelli, "Image quality assessment: from error visibility to structural similarity," *IEEE transactions on image processing*, vol. 13, no. 4, pp. 600–612, 2004.

[17] Boller and Chivens. (2020) 24-inch (.61 meter) telescope specifications. [Online]. Available: http://bollerandchivens.com/?p=2492

[18] AMS. (2020) CMV4000. [Online]. Available: https://ams.com/cmv4000

[19] Space-Track. (2020) ISS. [Online]. Available: https://www.space-track.org/#catalog

[20] NewTek Inc. (2020) Lightwave 3d 2020. [Online]. Available: https://www.lightwave3d.com

[21] NASA 3D Resources. (2020) Iss (high res). [Online]. Available: https://nasa3d.arc.nasa.gov/detail/iss-hi-res

[22] R. C. Dempsey, *The International Space Station: Operating an Outpost in the New Frontier*. Government Printing Office, 2017.

[23] R. K. Tyson, *Introduction to adaptive optics*. SPIE press, 2000.

[24] National Aeronautics and Space Administration. (2010) Reference guide to the international space station. [Online]. Available: https://www.nasa.gov/pdf/508318main_ISS_ref_guide_nov2010.pdf

[25] M. A. van Dam and R. G. Lane, "Wave-front sensing from defocused images by use of wave-front slopes," *Applied optics*, vol. 41, no. 26, pp. 5497–5502, 2002.

[26] F. Roddier, "Curvature sensing and compensation: a new concept in adaptive optics," *Applied Optics*, vol. 27, no. 7, pp. 1223–1225, 1988.

[27] European Space Agency. (2020) Envisat. [Online]. Available: https://www.esa.int/Enabling_Support/Operations/Envisat

[28] S. Weddell, R. Clare, and A. Lambert, "Near earth object image restoration with multi-object adaptive optics," in *Proc. 1st NEO and Debris Detection Conference*, 2019, pp. 22–24.